Optical Spectroscopy Study of Correlated Electron Physics in ABC-stacked Trilayer Graphene

by

Qihang Zhang

Bachelor of Science

Tsinghua University, 2018

Submitted to the Department of Electrical Engineering and Computer Science in Partial Fulfillment of the Requirements for the Degree of

Master of Science

at the

MASSACHUSETTS INSTITUTE OF TECHNOLOGY

February 2021

Author .....
Department of Electrical Engineering and Computer Science
January 8, 2021

Certified by .....
Long Ju
Assistant Professor of Physics
Thesis Supervisor

Accepted by .....
Leslie A. Kolodziejski
Professor of Electrical Engineering and Computer Science
Chair, Department Committee on Graduate Students

Optical Spectroscopy Study of Correlated Electron Physics in ABC-stacked Trilayer Graphene

by

Qihang Zhang

Submitted to the Department of Electrical Engineering and Computer Science on on Jan 8, 2021 in Partial Fulfillment of the Requirements for the Degree of Master of Science

Abstract

In recent years, people use 2D material as a building block to fabricate all kinds of multilayer stack devices, some of which host strongly correlated physics such as twist bilayer graphene and ABC-stack trilayer graphene. Mott insulator and superconductivity are found in these systems, which provide a cleaner and more controllable platform to study the strongly correlated physics than the traditional cuprate system. As a complementary method to transport measurement, which focuses on the low-frequency response, the optical spectrum is an important way to detect the frequency-dependent response and extract the underlying physics. In this project, we measured the optical spectrum on an ABC-stack trilayer graphene sample with the photocurrent method to understand the electron behavior in these delicate structures.

Thesis Supervisor: Long Ju

Title: Assistant Professor of Physic

Contents

1 Introduction **4**
- 1.1 background . . . 4
- 1.2 General idea . . . 4

2 Theory and Calculation **6**
- 2.1 Monolayer graphene . . . 6
- 2.2 Bilayer Graphene . . . 8
- 2.3 Trilayer Graphene . . . 16

3 Experiment and Equipment **19**
- 3.1 Optical absorption spectrum . . . 19
- 3.2 Fourier Transform Infrared Spectrometer . . . 20
- 3.3 Photocurrent measurement . . . 24
- 3.4 Cryostat and probe . . . 25

4 Experimental result **27**
- 4.1 Transport data of ABC-TLG . . . 27
- 4.2 Optical spectrum . . . 30
  - 4.2.1 Interband optical transitions at zero doping . . . 30
  - 4.2.2 Optical transitions in the mott phase . . . 34

5 Conclusion **38**

Chapter 1

Introduction

1.1 background

After the first stable 2D material, monolayer graphene, is discovered in 2004 [1], people entered the world of low-dimensional system. Unlike the quadratic dispersion for regular 3D materials, monolayer graphene has the Dirac shape k-E relationship with spin and valley degeneracy, which results in many exciting physics. With the development of the 2D material family, people use them as building blocks to make high quality samples, which can fine-tune the physical properties. In this way, a bunch of new behaviors emerged in this system.

Superconductivity found in twisted bilayer graphene by the Jarillo-Herrero group at MIT stirred the condensed matter physics community since it was announced in 2018 [2][3]. This is the first example to use engineered 2D materials to explore and study correlated electron physics that used to mainly happen in other condensed matter material systems. Since then, people use scanning tunneling microscope (STM) to detect the electronic structures of these strongly correlated twist bilayer-graphene samples[4][5][6][7]. However, for another important structure, ABC stack trilayer graphene, it is hard to study with STM because it has a top gate, which prevents scanning tips touch the sample directly[8][9]. Our infrared optical absorption spectrum method is suitable to measure the spectrum for this kind of structure with a top gate[10].

1.2 General idea

There are two common ways for infrared optical measurement, transmission and reflection. Since there is no good continuous laser in the mid-infrared and far-infrared range, we have to use a globar, a black body radiation source, as our light source for the optical spectrum. The smallest focused spot size from globar is about one millimeter. However, suppose we want to get a high-quality 2D material device. In that case, we need to encapsulated graphene into hexagonal boron nitride (hBN). This procedure limits the sample size to around 10 x 10 micrometers. If the beam spot is much higher than the sample size, the most signal comes from the silicon substrate rather than the sample

itself, so the optical noise is huge. It's very hard to get an optical spectrum with the traditional transmission and reflection method.

For the 2D material device, we can always tune the Fermi level with the bottom/top gate. If there is a gap in the sample, we can adjust the Fermi level into the gap to make the whole device lie in a low carrier density insolation state. If we shed light on our sample, photons will induce extra carriers in the system. This carrier density is proportional to the light absorption intensity. The idea of our photocurrent optical spectrum measurement is that we apply a small DC bias into the sample. After the photon-induced carrier appears, there will be a photon-induced current. This current is also proportional to light intensity. Fourier Transform Infrared Spectrometer (FTIR) is commercial equipment to measure infrared optical spectrum. It can produce an intensity-modulated output beam with a Michelson interferometer, which contains two mirrors. One is a fixed mirror, the other is a scanning mirror, output optical power is related to scanning mirror position. We use this equipment to shed light on the sample and collect the photocurrent signal as a function of scanning mirror position, after fourier transformation we will get the optical spectrum.

In this thesis, I will calculate the one, two, three layers graphene's band structure in Chapter.2, and discuss the origin of the strongly correlated properties in trilayer graphene. In Chapter.3, I will introduce the optical spectrum measurement and our photo-current experimental setup. In Chapter.4, I will put the transport result from our collaborator in ref.[8][9] back to back with our optical spectrum to interpret the data.

Chapter 2

Theory and Calculation

In this chapter, we will calculate the band structures of monolayer graphene, bilayer graphene and trilayer graphene. Monolayer graphene's band structure is relatively easier to get since it has an explicit solution, we will show the linear dispersion near the Fermi level at the conrner of brillouin zone. For multi-layer graphene, the inner plane has a covalent bond between C-C atoms, and the interlayer coupling is dominated by van deer walls interaction. We use the Linear Combination of Atomic Orbitals (LCAO) method to calculate AB-stack bilayer graphene's band structure and show a tunable electrical field induced band gap near the Fermi level. ABC-stack trilayer graphene also has electrical field induced gap, but the structure is more complicate, so we omit the intermediate procedure and directly put the result from self-consistent Hartree–Fock calculation.

2.1 Monolayer graphene

Monolayer graphene is part of the hexagonal crystal structure family with the crystal system being hexagonal rather than rhombo-hedral. The primitive unit cell is shown in Fig.2.1. Lattice constant for C-C bond is 1.42A.

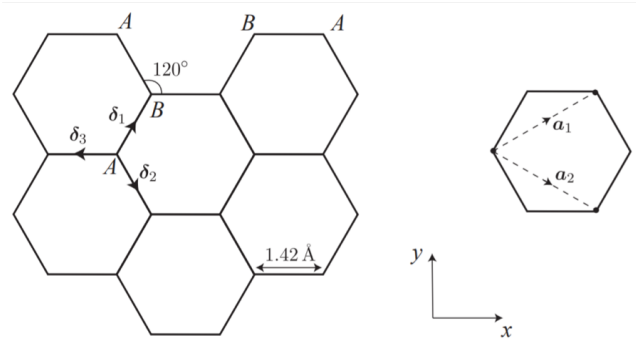

Figure 2.1: Unit Cell of monolayer graphene

.

The lattice is defined only in two dimensions, the primitive lattice vectors are shown in Fig.2.1, the first brillouin zone shape is shown in Fig.2.2, the high

symmetry point K and K' are also labeled.

$$\vec{a_1} = \left(\frac{a\sqrt{3}}{2}, \frac{a}{2}, 0\right)$$

$$\vec{a_2} = \left(-\frac{a\sqrt{3}}{2}, \frac{a}{2}, 0\right)$$

Reciprocal lattice vectors are defined according to the rule $\vec{a_i} \cdot \vec{b_j} = 2\pi\delta_{ij}$.

$$\vec{b_1} = 2\pi\left(\frac{1}{3a}, \frac{1}{\sqrt{3}a}, 0\right)$$

$$\vec{b_2} = 2\pi\left(\frac{1}{3a}, -\frac{1}{\sqrt{3}a}, 0\right)$$

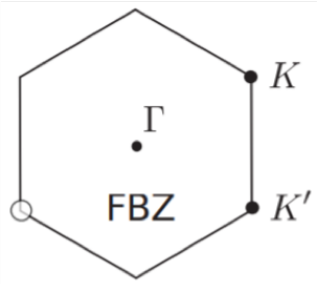

Figure 2.2: First brillouin zone of monolayer graphene

.

$$\vec{K} = 2\pi\left(\frac{1}{3a}, \frac{1}{\sqrt{3}a}\right)$$

$$\vec{K'} = 2\pi\left(\frac{1}{3a}, -\frac{1}{\sqrt{3}a}\right)$$

Considering the tight binding model with nearest neighbor interaction, the Hamiltonian can be written as

$$\hat{H}_{TB,n,n} = -t \sum_{ij=n.n} (a^{\dagger}_{i\sigma} b_{j\sigma} + H.c.)$$

After the Fourier Transform, we get

$$\begin{pmatrix} \alpha_k \\ \beta_k \end{pmatrix} = \sum_i \exp i\vec{k} \cdot \vec{R}^0_i \begin{pmatrix} a^{\dagger}_i e^{-i\vec{k}\cdot\vec{\delta_1}/2} \\ b^{\dagger}_i e^{i\vec{k}\cdot\vec{\delta_1}/2} \end{pmatrix}$$

$$\hat{H}_k = \begin{pmatrix} 0 & \Delta_k \\ \Delta^*_k & 0 \end{pmatrix}$$

where the

$$\Delta_k = -t \exp\left(-ik_x a\left(1 + 2\exp\left(i \cdot \frac{3k_x a}{a}\right)\cos\frac{\sqrt{3}}{2}k_y a\right)\right)$$

Now we can solve the eigen-equation and get the eigenvalue

$$\epsilon_k = \pm|\Delta_k| = \pm t\left(1 + 4\cos\frac{3k_x a}{a}\cos\sqrt{3}\frac{k_y a}{2} + 4\cos^2\frac{\sqrt{3}}{2}k_y a\right)^{\frac{1}{2}}$$

At K and K' point, the energy is 0, which means the Fermi level lies at K and K' point. Suppose $\vec{q} = \vec{k} - \vec{K}$, we substitute this formula into energy eigenvalue,

$$\Delta(\vec{q}) \simeq 2te^{-iK_x a}\vec{q}\cdot\nabla_k\left(e^{3ik_x a/2}\cos\frac{\sqrt{3}}{2}k_y a\right)_{\vec{k}=\vec{K}} = \hbar v_F(q_x + iq_y)$$

$$\hat{H} = \hbar v_F\begin{pmatrix}0 & q_x + iq_y\\ q_x - iq_y & 0\end{pmatrix} = \hbar v_F\hat{\sigma}\cdot\vec{q}$$

So the energy eigenvalue and eigenvector is

$$\epsilon(q) = \pm v_F|q|$$

$$\psi^{\pm}_{(K)}(q) = \frac{1}{\sqrt{2}}\begin{pmatrix}\exp i\theta_q/2\\ \pm\exp -i\theta_q/2\end{pmatrix}$$

$$\theta_q = \tan^{-1}(q_x/q_y)$$

Here we can clearly see that energy is proportional to the momentum, so it is a linear Dirac dispersion.

2.2 Bilayer Graphene

The two coupled honeycomb lattices in bilayer graphene (BLG) are misaligned from each other to lead to energetic stability of the bonds. The **lattice constant** of AB-stack BLG is identical to that of monolayer.

AB-stacked bilayer graphene is a 2D crystal consisting of two layers of Carbon atoms arranged in a hexeagonal lattice stacked at an offset to each other. The atomic configuration for Carbon (C) is as shown, C: $1s^2 2s^2 2p^2$.The valence electrons can be described by 2s and three 2p wavefunctions. As the interplanar interactions between the graphene are covalent, the outermost orbitals for bilayer graphene, with a basis of four atoms, is 16. These can be used to estimate the energy bands using the Linear Combination of Atomic Orbitals (LCAO) method. The Hamiltonian matrix for this approach will be a 16×16 matrix.

Graphene has an sp^2 hybridization, so the $2s$ orbital is mixed between the p_x and p_y orbitals, while the p_z orbital remains unhybridized. The hybridized orbitals constitute the σ-bond while the unhybridized orbital makes up the π-bond. The π-bonds hybridize to form the π and π^* bands which are responsible for most of graphene's unique properties [11]. We can represent these hybridized orbitals as a linear combination, giving the LCAO method credence.

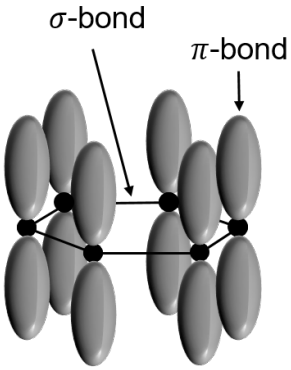

Figure 2.3: Monolayer graphene with the σ-bonds (black lines) and π-bonds formed by the p_z orbitals

Additionally, we could include core and unoccupied orbitals, up to the free electron energy, to better model our bands around the Fermi energy (E_F). The benefit of this comes from better representing a complete basis of an infinite number of bands compared to the finite basis proposed above. Doing this of course gives an untenable matrix to solve eigenvalues for. Adding the $1s$ core orbital increases the orbital basis to 20. The addition of this orbit would capture lower valence bands. However, has a negligible effect on those around the E_F due to the insignificant interactions between the $1s$ and $2s$ and $2p$ orbits. Adding the unoccupied bands would capture bands above those of the valence orbits but would have little effect on them due to them being empty at room temperature.

The primitive unit cell is shown in Fig.2.4. It has the same translational symmetry as in monolayer graphene but covers both layers and consists of four atoms: $A1$ and $A2$ in the bottom layer, $B1$ overlaying $A2$ and $B2$ in the top. The vertical layer separation is $d = 3.35$Å. Using the coordinate system as shown and taking $A2$ to be the origin, the basis vectors are given as

$$\vec{d_{A1}} = \left[\frac{a}{2}, \frac{a\sqrt{3}}{6}, 0\right]$$

$$\vec{d_{A2}} = [0, 0, 0]$$

$$\vec{d_{B1}} = \left[\frac{a}{2}, -\frac{a\sqrt{3}}{6}, d\right]$$

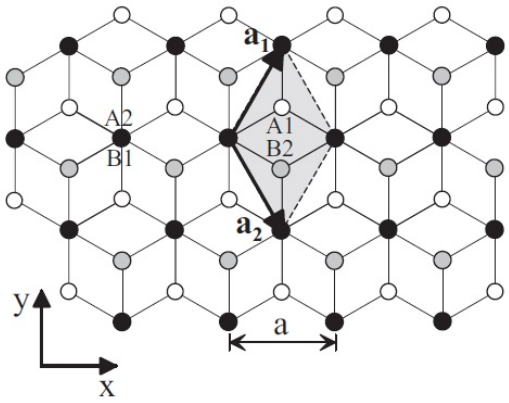

Figure 2.4: Unit Cell of bilayer graphene [12]

.

$$\vec{d_{B2}} = [0, 0, d]$$

The lattice is defined only in two dimensions, and primitive lattice vectors are also shown in Fig.2.4 and defined as

$$\vec{a_1} = \left(\frac{a}{2}, \frac{a\sqrt{3}}{2}, 0\right)$$

$$\vec{a_2} = \left(\frac{a}{2}, -\frac{a\sqrt{3}}{2}, 0\right)$$

Reciprocal lattice vectors are defined according to the rule $\vec{a_i} \cdot \vec{b_j} = 2\pi\delta_{ij}$.

$$\vec{b_1} = 2\pi\left(\frac{1}{a}, \frac{1}{\sqrt{3}a}, 0\right)$$

$$\vec{b_2} = 2\pi\left(\frac{1}{a}, -\frac{1}{\sqrt{3}a}, 0\right)$$

Fig.2.5 shows the xy-plane projection of the C atom orbitals, we need to check all interactions within a unit cell and drop the unimportant term to simplify our calculation.

$2s$-$2s$ interactions

As seen in Fig.2.6 the s-orbitals are spherically symmetric, the coupling terms will only differ by a phase. The two s-orbitals overlap to form a σ-bond such that $\langle\phi_{s_1}|\,\hat{H}\,|\phi_{s_2}\rangle = V_{ss}$.

$2s$-$2p_i$ interactions

The s-p interactions are attributed to the $2s$ and $2p_i$ orbitals. Since the p_i orbitals have polarity associated to them, the interactions will have a sign and

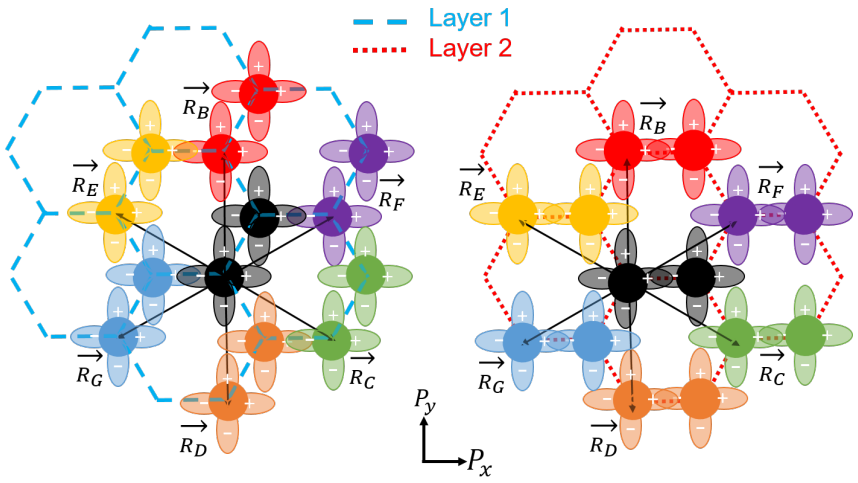

Figure 2.5: A 2D view of the lattice with the s, p_x, and p_y orbitals

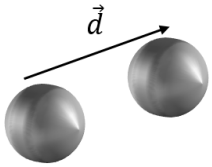

Figure 2.6: s-s orbital interactions

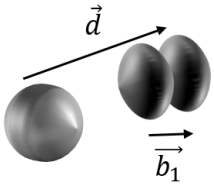

Figure 2.7: s-p_1 interaction

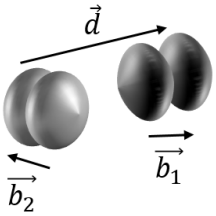

Figure 2.8: p_1-p_2 interaction

a phase dependence. Two vectors $\vec{d}$ and $\vec{b_1}$ represent the unit vector from one carbon atom to the other carbon atom and the unit vector from the negative to positive lobe of the p_i-orbital, respectively. Generally, $\langle \phi_s | \hat{H} | \phi_{p_i} \rangle = V_{sp}(\vec{d} \cdot \vec{b_1})$. See fig. 2.7 for the diagram of the s-p interaction.

$2p_i$-$2p_j$ interactions

The p-p interactions are attributed to the $2p_i$ orbitals. Three vectors $\vec{d}$, $\vec{b_1}$, and $\vec{b_2}$ represent the unit vector from one carbon atom to the other carbon atom, the unit vectors from the negative to positive lobe of the p_i-orbital ($\vec{b_1}$), and p_j-orbital ($\vec{b_2}$), respectively. However, this interaction will have two components depending on how the orbitals are aligned. Generally, $\langle\phi_{p_i}|\hat{H}|\phi_{p_j}\rangle = V_{pp\sigma}(\vec{d}\cdot\vec{b_1})\cdot(\vec{d}\cdot\vec{b_2}) + V_{pp\pi}[\vec{b_1} - \vec{d}(\vec{b_1}\cdot\vec{d})]\cdot[\vec{b_2} - \vec{d}(\vec{b_2}\cdot\vec{d})]$. See fig. 2.8 for the diagram of the p-p interaction. Finally, note that due to the uniformity of the graphene lattice, and all the atoms in the basis being C, the LCAO approximation allows for $\left\langle\phi_{2s}^{A1}(\vec{R_A})\right|\hat{H}\left|\phi_{2px}^{A2}(\vec{R_B})\right\rangle = \left\langle\phi_{2s}^{A2}(\vec{R_A})\right|\hat{H}\left|\phi_{2px}^{A1}(\vec{R_B})\right\rangle$ and $\left\langle\phi_{2s}^{A1}(\vec{R_A})\right|\hat{H}\left|\phi_{2s}^{A1}(\vec{R_A})\right\rangle = \left\langle\phi_{2s}^{A1}(\vec{R_B})\right|\hat{H}\left|\phi_{2s}^{A1}(\vec{R_B})\right\rangle$. After solving the full 16x16 Hamiltonian, we get the band structure like shown in Fig.2.9. However, the Hamiltonian for AB graphene can be reduced to capture the just the π-bands which are closest to the Fermi level and the Dirac point. As shown below, all the p_z orbitals columns are gathered and the V_{sp} terms are taken to be 0. Shown in fig. 2.10 is the band structure for M-Γ-K-M-Γ.

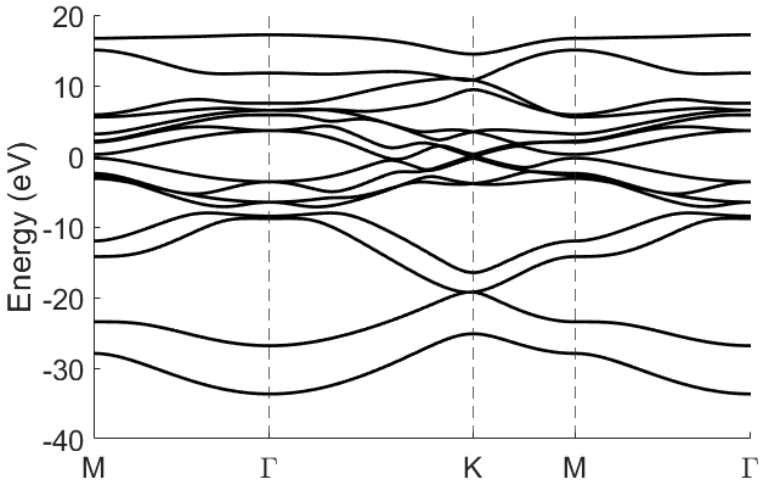

Figure 2.9: The full band structure using the LCAO method

$$\begin{array}{c} \begin{matrix} |\phi_{A1,p_z}\rangle & |\phi_{A2,p_z}\rangle & |\phi_{B1,p_z}\rangle & |\phi_{B2,p_z}\rangle \end{matrix} \\ \begin{bmatrix} E_p & V_{pp\pi}g_0 & 0 & V_{sp} \\ V_{pp\pi}g_0^* & E_p & 0 & V_{pp\sigma} \\ 0 & V_{sp} & E_p & V_{pp\pi}g_6 \\ 0 & V_{pp\sigma} & V_{pp\pi}g_6^* & E_p \end{bmatrix} \end{array} \begin{matrix} \\ \\ 0 \\ 0 \end{matrix}$$

Using this reduced Hamiltonian, we show a surface plot for a range of (k_x, k_y) coordinates in k-space, as shown in Fig. 2.11 for the bands closest to the Fermi energy. The wavefunctions closest to the Fermi energy are only

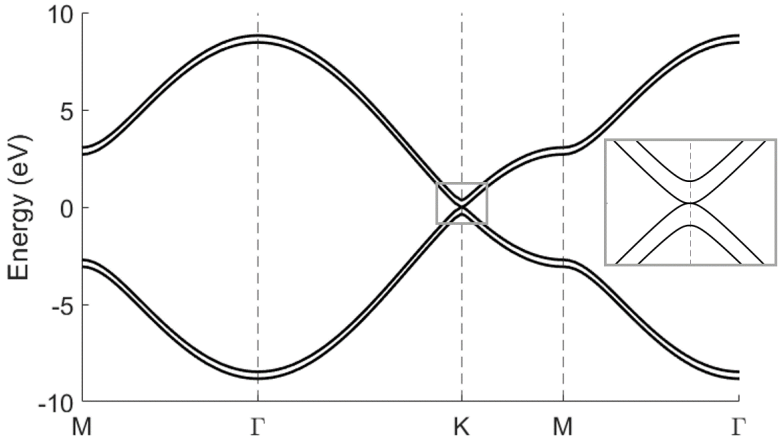

Figure 2.10: The reduced band structure from M-Γ-K-M-Γ

given by the p_z orbitals of the A1 and B1 atoms. Thus transport is dominated by the p_z electrons of those two atoms which don't have out of plane orbital overlaps.

$$\Psi_{VB}(r) = \phi_{B_1,p_z}(r)$$

$$\Psi_{CB}(r) = \phi_{A_1,p_z}(r)$$

The other two bands are linear combination of the p_z orbitals of A_2 and B_2 which have the out of plane interaction and are further from the Fermi level. The highest energy level is when the two atoms have wavefunctions which are out of phase.

$$\Psi_{h'}(r) = \frac{1}{\sqrt{2}}\left(\phi_{A_2,p_z}(r) + \phi_{B_2,p_z}(r)\right)$$

$$\Psi_{e'}(r) = \frac{1}{\sqrt{2}}\left(\phi_{A_2,p_z}(r) - \phi_{B_2,p_z}(r)\right)$$

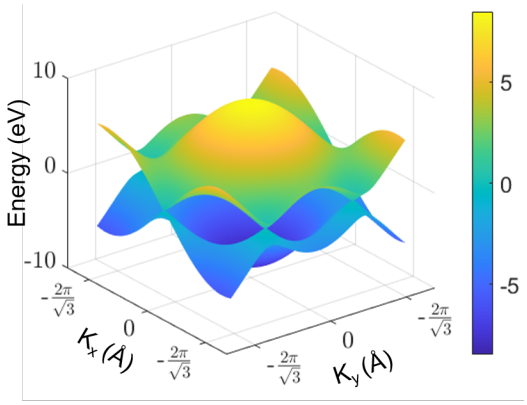

Figure 2.11: Surface plots of conduction and valence bands, including the six Dirac points

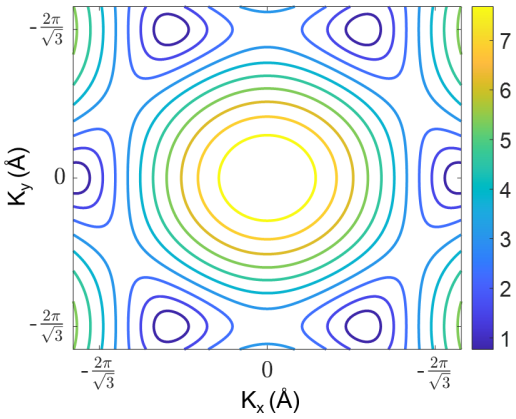

Figure 2.12: |E|-k contour plot, showing the six Dirac 'pockets'

Tunable Bilayer Graphene Band Structure

One of the reasons that make bilayer graphene an interesting material is that it has a tunable bandgap. First reported in Nature in June 2009, Yuanbo Zhang and coworkers, experimentally demonstrated this phenomena. They used a top and bottom gate to tune the displacement field in each of the graphene layers, which allows for electron or hole doping depending on the applied bias. See fig. 2.13 for a schematic. For our LCAO model, we also demonstrate this tunable bandgap by changing the top two E_p in the reduced Hamiltonian to control the Fermi energy of the top layer and the bottom two E_p to control the bottom layer. Choosing $|E_p| = 0.2$ eV, we get a gap opening of 175 meV; $|E_p| = 0.4$ eV, we get a gap opening of 260 meV; and $|E_p| = 1.0$ eV, we get a gap opening of 335 meV. See fig. 2.14. With low $|E_p|$, there is small band bending at the Dirac point, when $|E_p|$ is increased, the gap becomes larger and the curvature of the bands starts to become wider. The largest bandgap observed in the paper was 250 meV. They also performed and provided a comparison of their experimental data and theoretical predictions seen in fig. 2.15. Our model is equivalent to the unscreened tight-binding as we change the $|E_p|$, we obtain a linear change in the bandgap. In self-consistent tight-binding, additional variables are added by considering many other nearest neighbors in and out of plane.

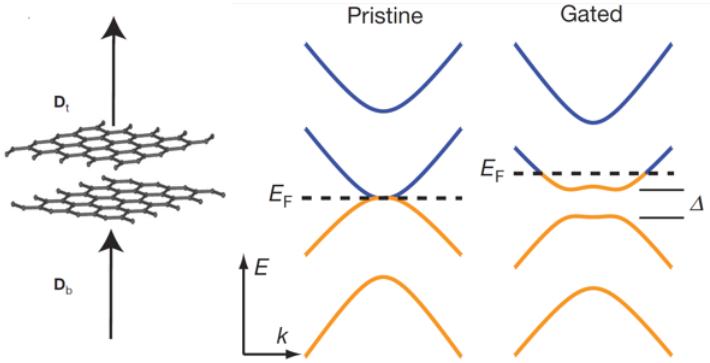

Figure 2.13: Sketch showing how gating of the bilayer induces top (D_t) and bottom (D_b) electrical displacement fields. The left band stucture shows the electronic structure of a pristine bilayer has zero bandgap. On the right, upon gating, the displacement fields induces a non-zero bandgap Δ [13]

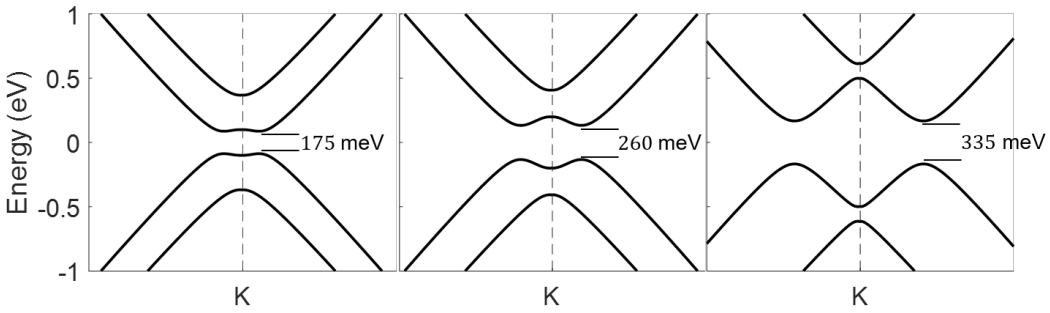

Figure 2.14: The band structure of bilayer graphene at (from left to right) $|E_p| = 0.2$ eV, $|E_p| = 0.4$ eV, and $|E_p| = 1.0$ eV

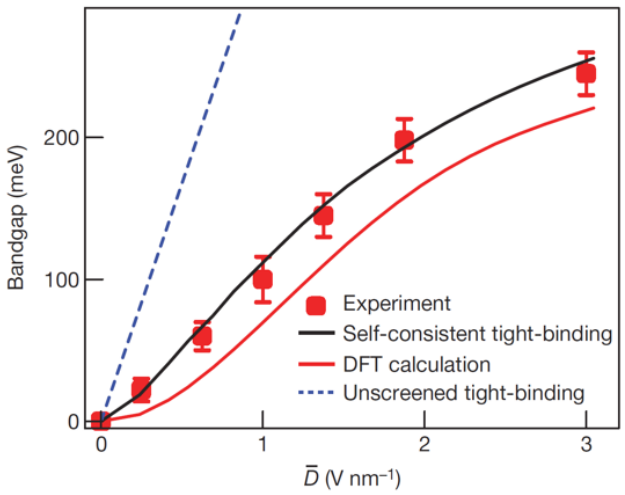

Figure 2.15: A comparison of experimental data and theoretical models from [13] showing the bandgap dependence on displacement field

2.3 Trilayer Graphene

Why do we want to add one more layer on BLG? Because we want to search the strongly correlated physics in graphene system. The competition between the bandwidth (W) and the Coulomb repulsion energy (U) is a well-known explanation of the mott insulator. Bandwidth has a positive correlation with the kinetic energy gain of an electron via hopping to the neighbor sites, the more kinetic energy gain, the easier to delocalize an electron's wave function. If the neighbor site also has electrons, there will be coulomb energy to repulse the new electron, this mechanism tend to make electrons localized. The regular band theory will not include Coulomb energy because they only consider electron and lattice interaction rather than the interaction between electrons, which is called single electron assumption. If electron density is high enough, electrons will screen each other to reduce the effective Coulomb energy. If we reduce the density of electrons, although the average distance is larger, the screen effect is weaker, so the overall effect results in the increase of the Coulomb energy. If Coulomb repulsion energy is well larger than bandwidth, electrons localized, and the material is in an insulating state called mott insulator.

Monolayer graphene has linear dispersion near the Fermi level, bilayer graphene changes to quadratic dispersion, a pretty natural question is that "will the trilayer graphene be even flatter?" The answer is true. In this case, we apply an electrical field to open a gap, which can further press the band to be flatter. Moreover, we can align the bottom layer graphene with the hBN substrate to create a morie superlattice, this method can open a moire gap and dilute the local electron density. In this way, we can push the physical property of TLG system into strongly correlated domain. Now let's have the quantitatively examine of bandwidth and Coulomb repulsion energy.

For the ABC-TLG/hBN heterostructure with an $L_M = 15nm$ moiré superlattice, the single-particle bandstructure of the heterostructure is described by the Hamiltonian $H = H_{ABC} + V_M$, where H_{ABC} is the ABC-TLG Hamiltonian under a weak vertical electrical field, and V_M describes the effective potential acting on ABC-TLG from the moiré superlattice. The low-energy electronic structure of the ABC-TLG can be captured by an effective two-component Hamiltonian in the K valley that describes hopping between the A atom in the top graphene layer and the C atom in the bottom graphene layer[8]:

$$\begin{aligned} H_{ABC} =& \frac{v_0^3}{t_1^2}\begin{pmatrix} 0 & (\pi^+)^3 \\ \pi^3 & 0 \end{pmatrix} + \left(\frac{2v_0v_3p^2}{t_1} + t_2\right)\sigma_1 \\ &+ \left(\frac{2v_0v_4p^2}{t_1} - \Delta'\right) I \\ &+ \left(\frac{3v_0^2p^2}{t_1^2} - 1\right)\Delta'' I - \Delta\sigma_3 \end{aligned}$$

where $\pi = p_x + ip_y$, p is the electron momentum, $U = 2\Delta$ is the electron energy difference between the top and bottom layer due to the vertical electrical field. $v_i = \frac{\sqrt{2}}{2}at_i/\hbar$, $a = 2.46A$ is the carbon–carbon lattice constant,

$\Delta' = 0.00122eV$, $\Delta'' = -0.0095eV$ and t_0, t_1, t_2, t_3 and $t4$ are tight binding parameters in ABC-TLG obtained from local density approximation (LDA) ab initio calculations with values of $2.62, 0.358, 0.0083, 0.293$ and $0.144eV$, respectively[8]. The dispersion plot with different U value (from -200mV to 150mV) are attached in Fig.2.16 and Fig.2.17, the negative U means the external electrical field is applied from an opposite direction.

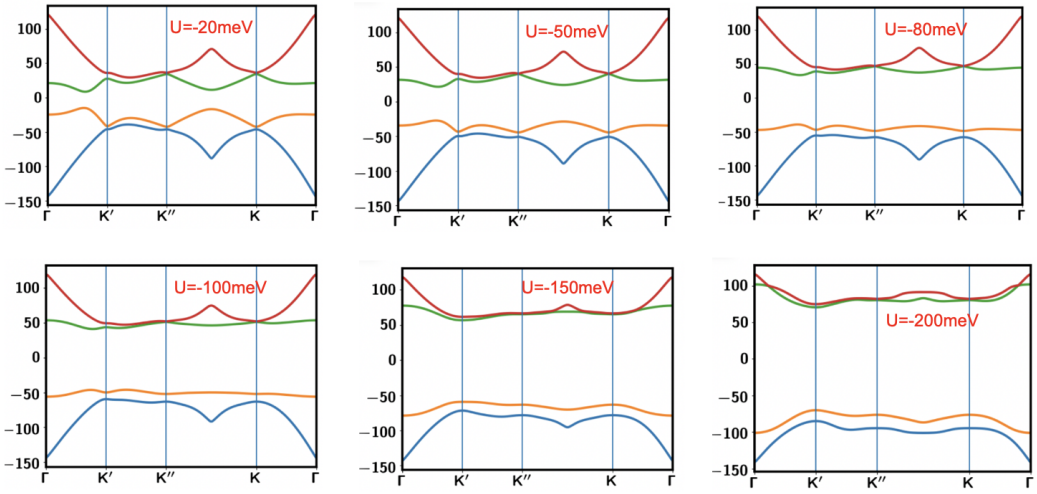

Figure 2.16: Band structure of TLG with external electrical field, $U = [-2000meV, -20meV]$

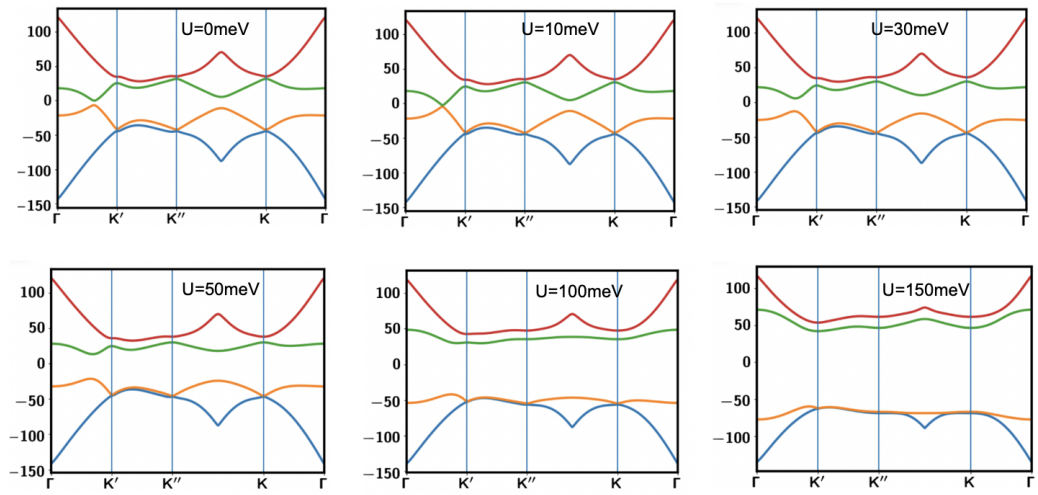

Figure 2.17: Band structure of TLG with external electrical field, $U = [0meV, 150meV]$

From the band structure plots, we can learn the following things. (a) the band gap at charge neutral point is proportional (equivalent) to U for ABC-TLG. (b) Bandwidth will decrease as the U increase until U is so big ($> 100meV$) that distorts flat band, as shown in Fig.2.18

(c) At $U = 20meV$, We observe that the first hole miniband is strongly suppressed by the vertical field and has $W \approx 13meV$.The on-site Coulomb repulsion energy can be estimated by $U \approx \frac{e^2}{4\pi\epsilon_0\epsilon L_M}$, For $L_M = 15nm$ and an hBN dielectric constant $\epsilon = 4$, U is $\sim 25meV$, which is larger than the value of W [8]. This dominating on-site Coulomb repulsion naturally leads to Mott insulator states in the isolated hole mini-band when there are one or two holes per site, that is, at 1/4 and 1/2 filling of the band.

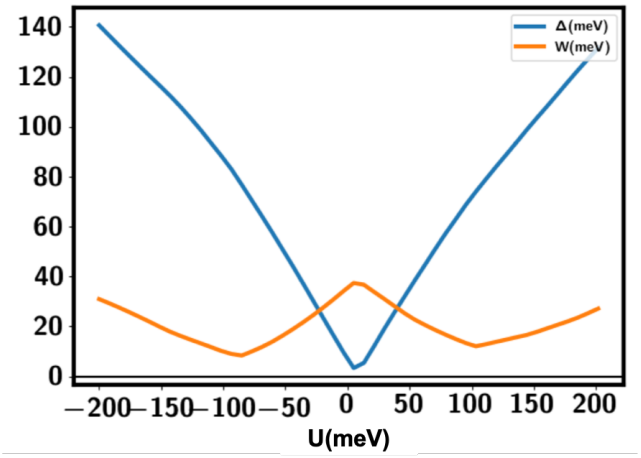

Figure 2.18: U dependent plot of band gap Δ and bandwidth W

Chapter 3

Experiment and Equipment

3.1 Optical absorption spectrum

Light-matter interaction play an important role in both fundamental physics and applications, so optical spectroscopy is an useful method to detect the physical properties in the material. Electron-photon scattering is essentially the response to an AC electrical field with a frequency ω. The optical spectrum can provide information about frequency-dependent response to the external field, it is different from the transport measurement, which shows the response to a low-frequency (static) external field. Both transport and optical spectroscopy require the external field to be weak to keep the perturbation theory valid and prevent the nonlinear effect.

In this section, we only consider single electron-photon scattering process. Both energy and momentum are conserved in this case.

$$E_{i,e} + \hbar\omega_i = E_{f,e} + \hbar\omega_f$$

$$\vec{p}_{i,e} + \hbar\vec{k}_i = \vec{p}_{f,e} + \hbar\vec{k}_f$$

Where i and f is on behalf of initial and final state. Since the speed of light c is much higher than the speed of electrons in the material, within the low energy regime, we can always assume $\hbar|\vec{k}| \ll \vec{p}_e$, the $\hbar\vec{k}_i$ and $\hbar\vec{k}_f$ term can be neglected. The optical absorption is an electron absorb a photon and transit to a higher energy level. The electron's optical transition always happens at the same momentum.

$$E_{i,e} + \hbar\omega = E_{f,e}$$

$$\vec{p}_{i,e} = \vec{p}_{f,e}$$

Absorption efficiency depends on the interaction formula, Fermi level and the band structure. It follows the Fermi golden rule.

$$\gamma = \frac{2\pi}{\hbar}|V|^2\rho$$

$$V = \left\langle \phi_i \left| \hat{H}_{int} \right| \phi_f \right\rangle$$

$$\rho = f(E_i)(1 - f(E_f))$$

where γ is the transition probability per unit time, V is the interaction strength between initial and final state, $\hat{H}_{int}$ is the interaction Hamiltonian, ϕ_i and ϕ_f are wave functions of initial and final state, ρ is the joint density of state, $f(E) = \frac{1}{1+\exp\frac{E-\mu}{kT}}$ is the Fermi-Dirac distribution, μ is chemical potential, in the most low temperature case, μ is equal to E_F.

Transition probability is proportional to the joint density means that the optical transition is allowed only when the initial state has one electron and the final states is empty, this is a result of Pauli repulsion principle.

An example for monolayer graphene absorption in visible range is shown in Fig.3.1[14].

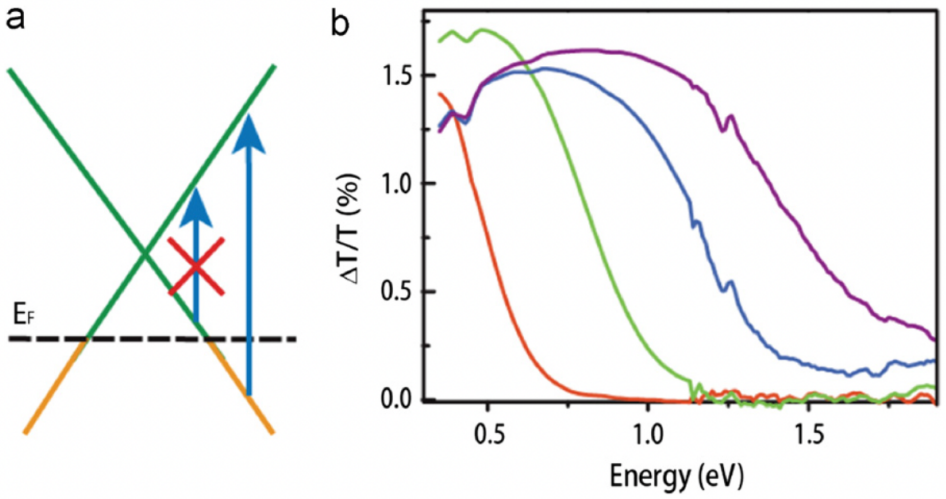

Figure 3.1: Gate-tunable interband transitions in graphene: (a) an illustration of interband transitions in hole-doped graphene. Optical transitions at photon energies greater than $2\epsilon_F$ are allowed, while those at energies below $2\epsilon_F$ are blocked. (b) the gate-induced change of transmission in hole-doped graphene as a function of gate voltage V_g. The values of the gate voltage referenced to that for charge neutrality, $V_g - V_{CNP}$, for the curves -0.75, -1.75, -2.75 and -3.5 eV, from left to right. consistent[14]

3.2 Fourier Transform Infrared Spectrometer

Fourier Transform Infrared Spectrometer (FTIR) is a commercial product to measure the optical absorption spectrum in the infrared range. It includes the light source, interferometer and detector.

Light source

FTIR use globar as the light source. Globar is a black body radiator with $\sim 1500K$ surface temperature. The blackbody radiation spectrum is shown in

Fig.3.2, from that we know 1500K radiation has peaks on near-infrared(NIR), covers the mid-infrared)(MIR and has a tail on far-infrared(FIR). Our research interest focus on FIR range, so we need a low-pass filter to filter out high energy photon to prevent the heating and photo-doping effect. Moreover, the short of intensity at FIR range limit the application of FTIR in low energy system, the signal is too weak to extract from noise.

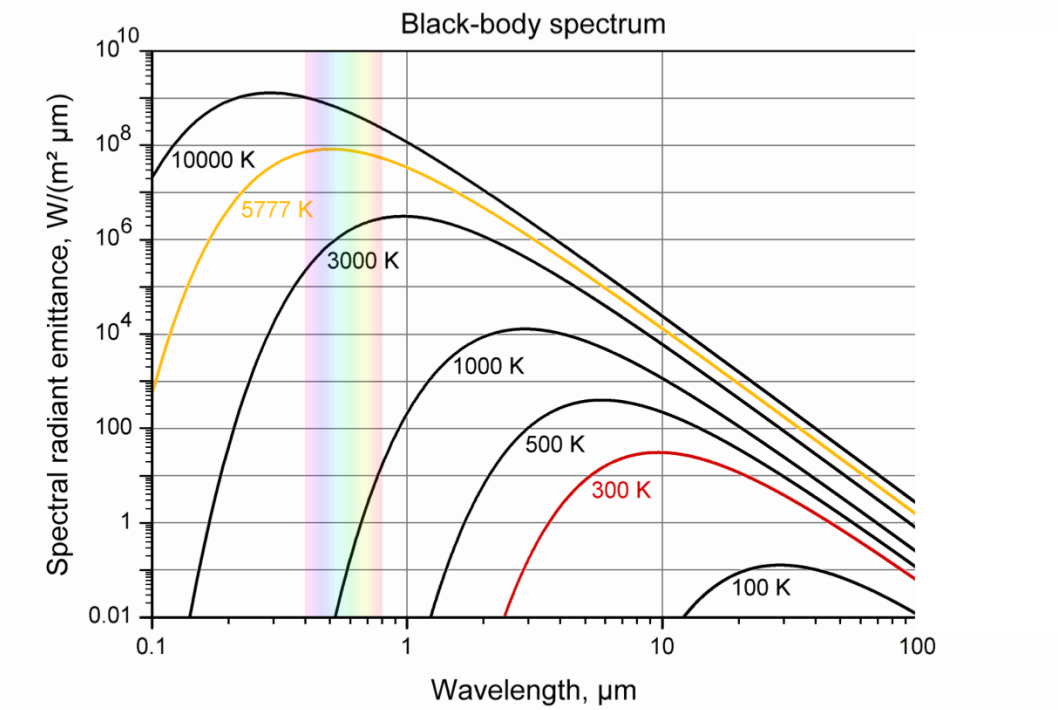

Figure 3.2: Black body radiation spectrum with different surface temperatures.

Interferometer

The structure of FTIR is shown in Fig.3.3, we don't use any lens in the beam path because the transmission and chromatic aberration are unsatisfactory for lens in IR range. Light from globar is collimated by a parabolic mirror, and then enter the interferometer. The beam is splitted by the beam splitter and reflect by two mirrors. One mirror is fixed, the other one is movable. The reflected beams recombine at beam splitter and go to the output port. The output beam is the interference of the beam from two benches, so its intensity is modulated by the optical distance difference of the two benches.

For transmission setup, the output collimate beam is focused on sample and then reach the detector finally. We normalize the spectrum with sample by the spectrum without sample to remove the systematic spectrum shape such as the spectrum of light source, beam splitter and detector.

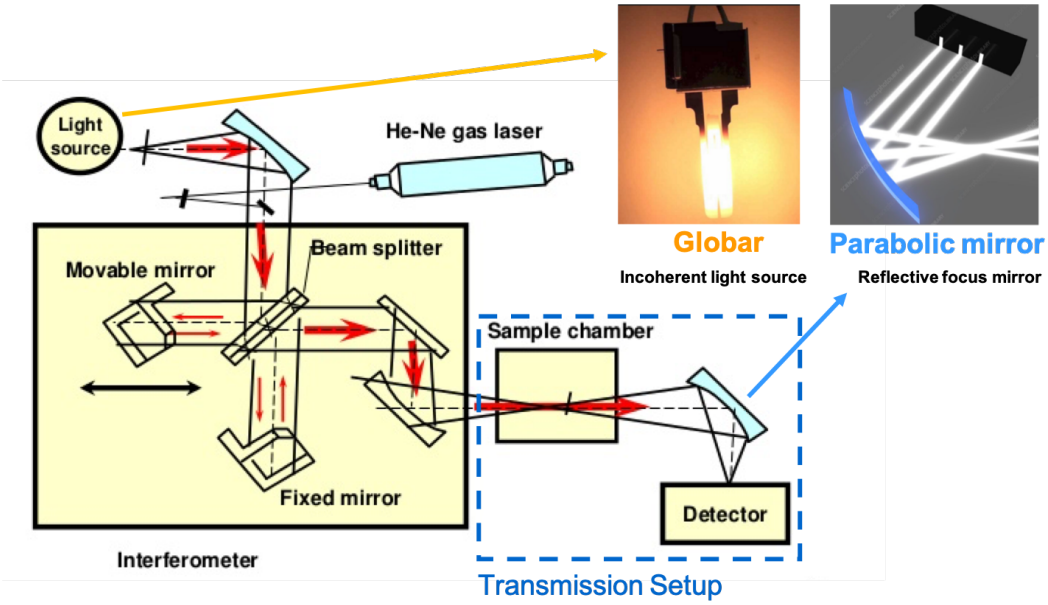

Figure 3.3: The sketch of FTIR.

Interferogram and spectrum

Now let's discuss about how to get a spectrum from FTIR. Fig.3.4 shows the optical beam path of the Michelsons interferometer.

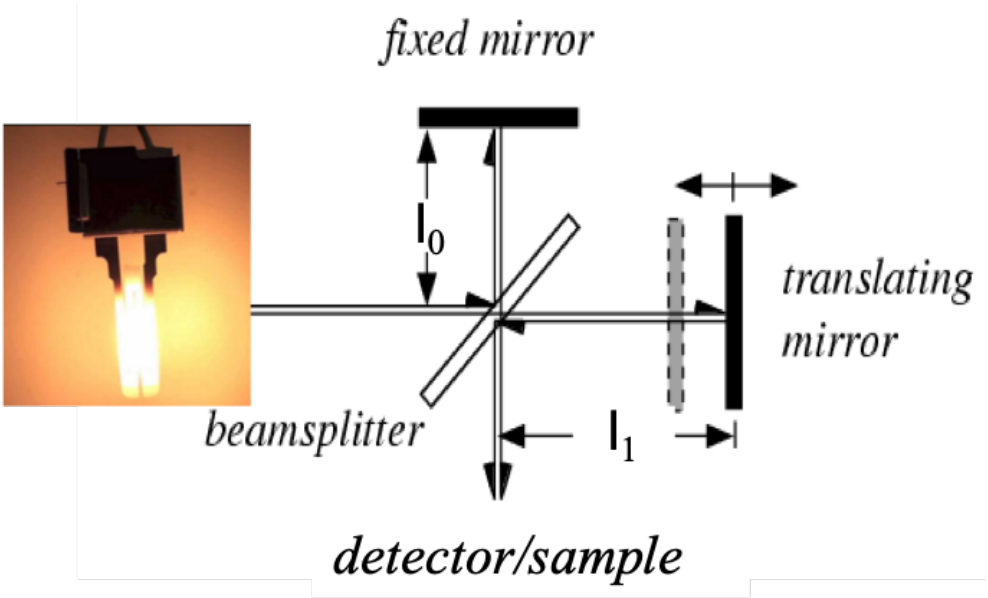

Figure 3.4: The beam path of Michelsons interferometer.

We assume l_0 is the arm length of the fixed mirror, l_1 is the arm length of the translating mirror. The output intensity at wave vector k is a function of

l_1,

$$I_{output}(k, l_1) = EE^* \propto \left|e^{i\omega t+ikl_1} + e^{i\omega t+ikl_0}\right|^2$$
$$= 2 + 2\cos k(l - l_0)$$

The detector can only detect the total optical intensity,

$$I(l) = \int [2 + 2\cos k(l - l_0)]\, \phi(k) dk$$

$I(l)$ is the interferogram collected by the detector, and $\phi(k)$ is the spectrum we want to get. Fig.3.5 shows an example of the interferogram.

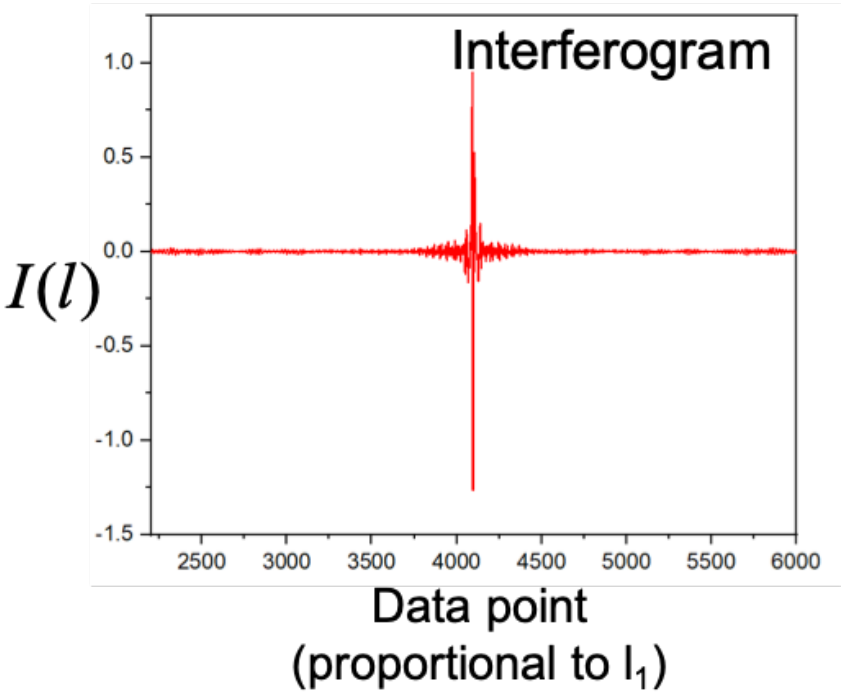

Figure 3.5: Example: an interferogram of a bare MCT dector.

After the fourier transform, we get

$$\phi(k) = \int I(l)\cos(kl) dl$$

Fig.3.6 shows the corresponding spectrum of the interferogram of Fig.3.5.

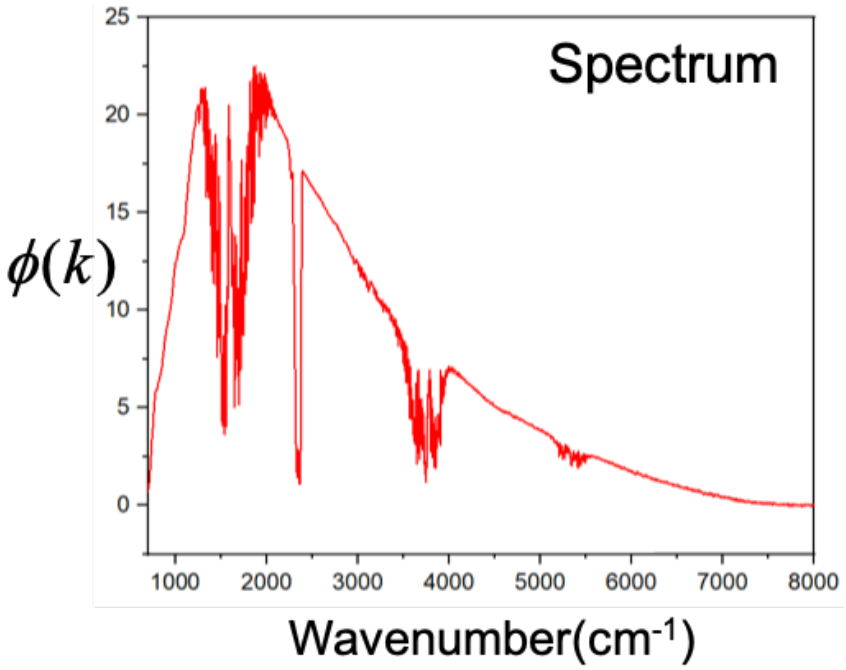

Figure 3.6: Example: The fourier transform of the interferogram, it is the spectrum corresponding to the bare MCT dector.

3.3 Photocurrent measurement

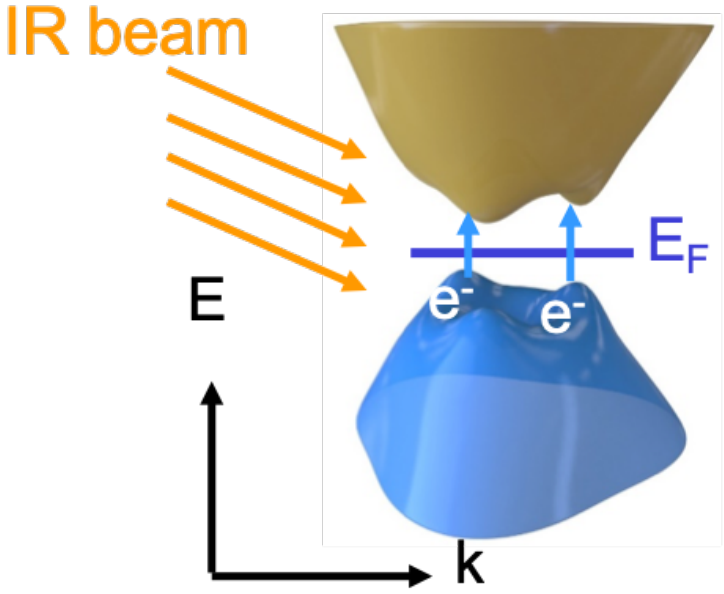

Figure 3.7: Sketch of the interband transition in BLG, when Fermi level lies in the gap.

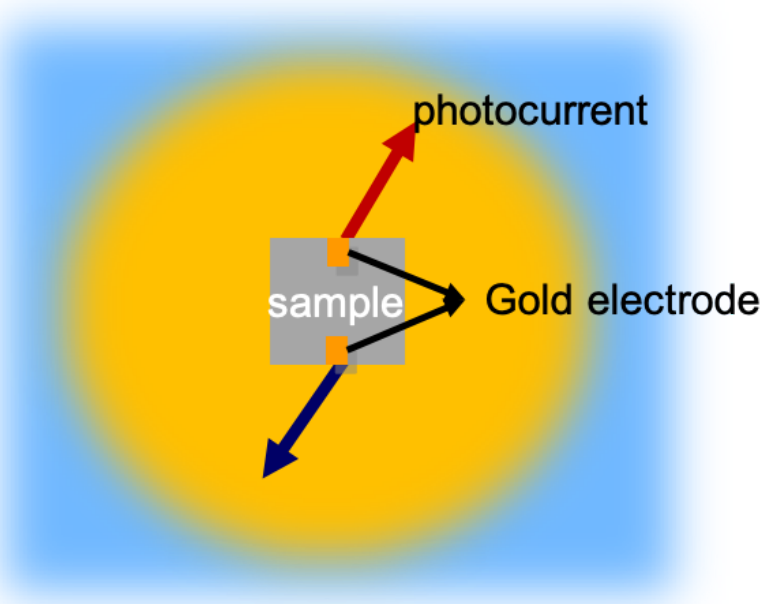

Figure 3.8: The photon-induced carrier is collected by the electrode fabricated on the sample.

3.4 Cryostat and probe

We use a low temperature, high field superconductor magnet cryostat for this optical spectrum measurement, in this work we don't need high magnetic field, but we can carry out high field magneto-optical measurement in this system. Our cryostat utilizes the variable temperature insert (VTI) design, the magnet and VTI are buried in the liquid helium environment. VTI's inside sample space is separated by a vacuum jacket from the the liquid helium environment, typically the vacuum jacket is pumped down to 1E-5 mbar to maintain the thermal isolation. A capillary tube connects the inside and outside space of the VTI, we can pump the sample space to suck the helium from the outside to cool down the sample space, a needle valve is installed on the end of this capillary tube to apply a precise control of helium flow. A heater is attached to the bottom of the VTI to heat it up, in this way, we can control the VTI's temperature, that's why it is called variable temperature insert. Liquid helium evaporation temperature is 4.2K, if we pump the liquid helium, the helium drop will evaporate in the sample space and take out more heat, so the lowest temperature in our system is around 1.2K.

Typically the cryostat is designed for transport measurement, which only requires electrical connections. But we have to guide the IR beam to focus on the sample in the optical experiment, so we designed a special probe to meet the requirement. We utilize a copper tube as the main part of our probe, the inner surface of this copper tube is polished to guide the beam. Although copper has a higher thermal conductivity compared to 304 stainless steel, which

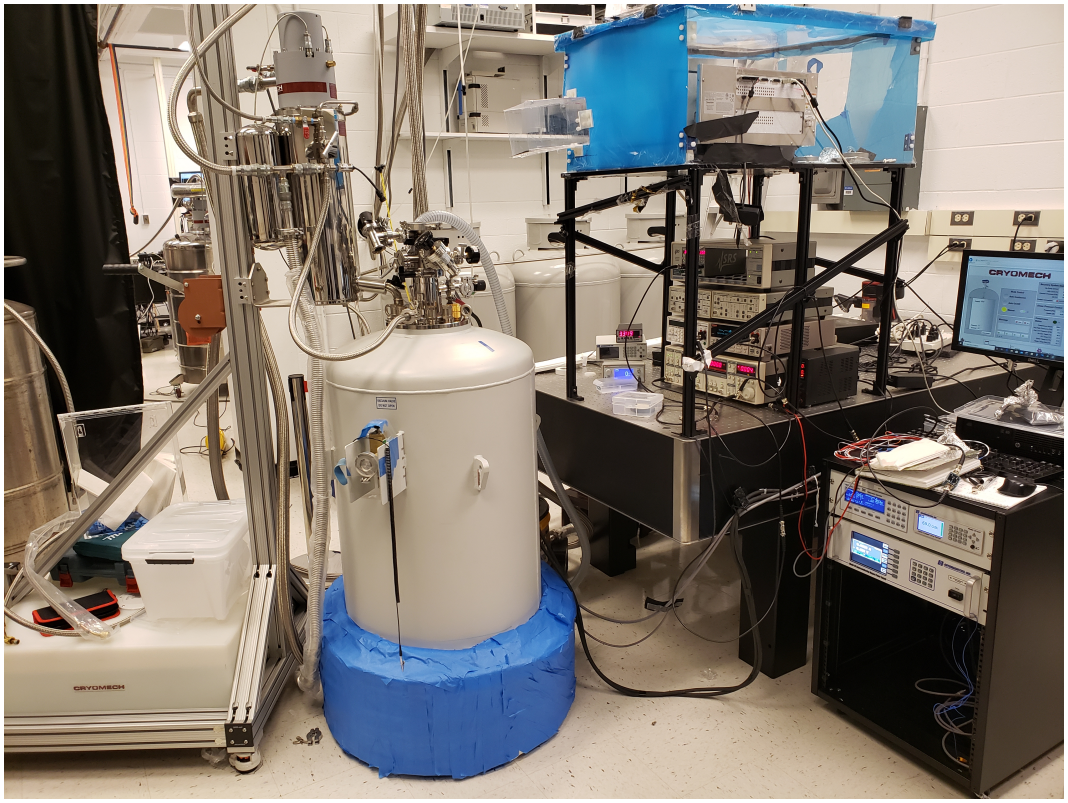

Figure 3.9: Overview of our cryostat.

could result in a higher base temperature at sample space, we choose copper because it has a higher reflectively to get a stronger light power on the sample. On top of the probe we cap it with a diamond window to seal the vacuum, diamond has uniform transparency in IR range, it is suitable for all-purpose measurement. On the side we put two 19-pin military connectors and a valve to make the electrical wiring and vacuum pumping port. Since the lens in IR range is limited by the material, we can't find broadband, low chromatic aberration lens that works at low temperature, we use a reflective Winston cone to focus IR beam down to around 1mm spot on the sample.

Chapter 4

Experimental result

4.1 Transport data of ABC-TLG

In this section, I will introduce the transport data of TLG from our collaborators in ref.[9]. In our project, we measured the same sample as in ref.[9].

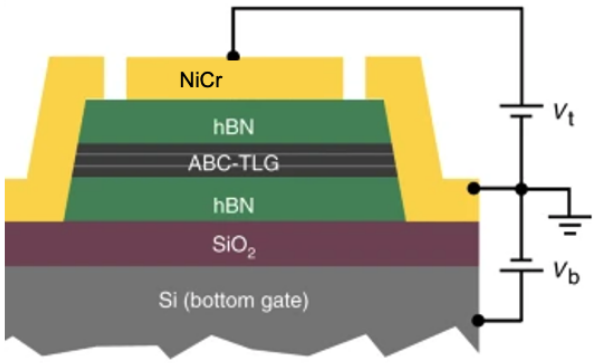

Figure 4.1: Schematic cross-sectional view of the device.[8]

In this device, ABC-TLG is encapsulated by two hBN layers, this sandwich structure lies on a SiO_2/Si chip, SiO_2 thickness is around 290nm, Silicon serves as the bottom gate. Gold electrodes is deposited on the side of the device to make a good contact to TLG layer. A NiCr gate layer is capped on the top of the device, NiCr is an IR transparent material so it will not block our IR beam coming from the top.

The bottom layer of ABC-TLG is aligned with the top layer of the bottom hBN to form the moiré superlattice as shown in Fig.4.2. This superlattice is a triangular lattice with the moiré wavelength around 15nm in this device. Due to the spin and valley degeneracy, each site can host at most 4 electrons(or holes) in one band. We can tune both the filling factor and the displacement field with top and bottom gates.

When the filling factor of the mini-band is 1/2, each superlattice site contains two electrons(or holes) as shown in Fig.4.3, the on-site coulomb repulsion U prevents them from hopping to each other, this insulation state is called mott

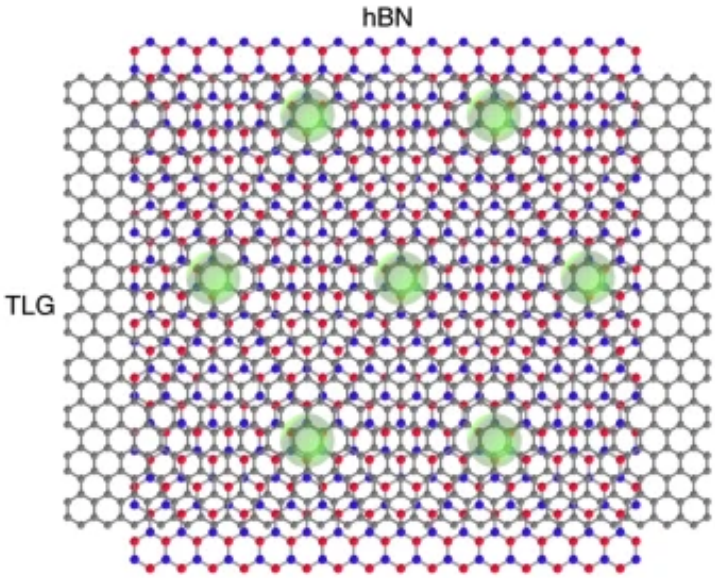

Figure 4.2: Schematic of ABC-TLG/hBN moiré superlattice. Gray dots are the bottom graphene layer atoms, while the red and blue dots are the atoms of the top hBN layer.[8]

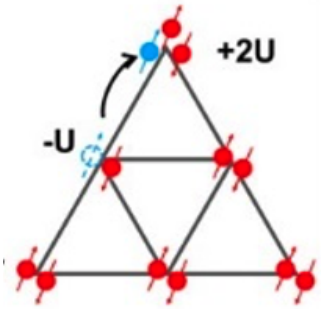

Figure 4.3: In the Mott insulating state at half filling, each superlattice site contains two electrons(or holes) and they are separated by the dominating Coulomb repulsion.

insulation state. From the DOS plot, the conduction band is a continuous band when filling factor is 0. When we tune the Fermi level to 1/4 and 1/2 filling, extra mott gap is induced since an electron need more energy to compensate the coulomb energy cost as shown in Fig.4.4.

Fig.4.5 shows the 2D color plot of the R_{xx} as a function of top gate voltage V_t and bottom gate voltage V_b at 5K temperature. x and y axis are re-scaled to align the constant carrier density n to diagonal direction and constant displacement field D to off-diagonal direction. We can clearly see that there are two extra resistance peaks show up corresponding to the 1/2 and 1/4 filling factor with a relative big displacement field. The appearance of 1/2 and 1/4 filling peak indicate that the displacement field induced gap can suppress the valance band width to enhance the strongly correlated physics. the A weaker line lies at the bottom left of the plot is the full filling peak of mini-band.

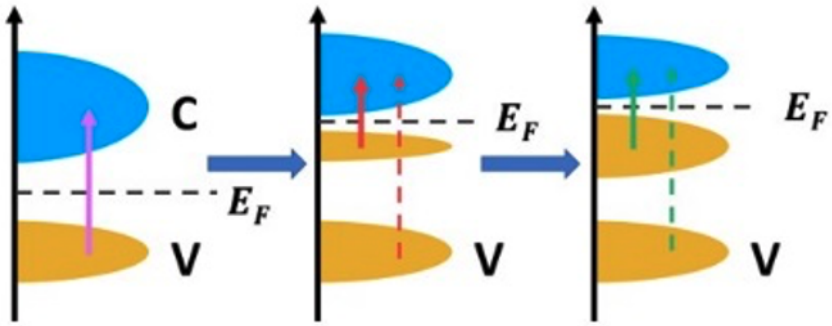

Figure 4.4: Two band model of mott insulator. When the Fermi level lies in the full filling position, sample behaves like a normal insulator. When we turn the Fermi level into the 1/2 and 1/4 filling factor, on-site coulomb repulsion dominate the properties, a strong correlated gap is induced in the conduction band.

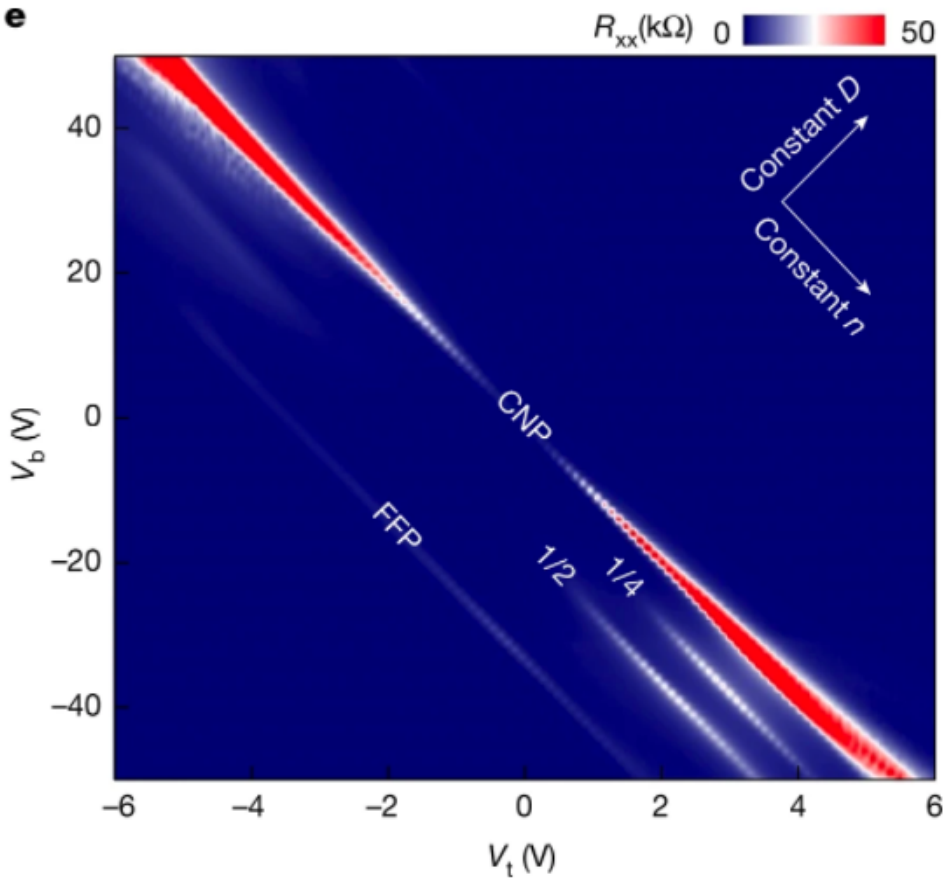

Figure 4.5: Two-dimensional color plot of Rxx as a function of Vt and Vb at T = 5 K. [9]

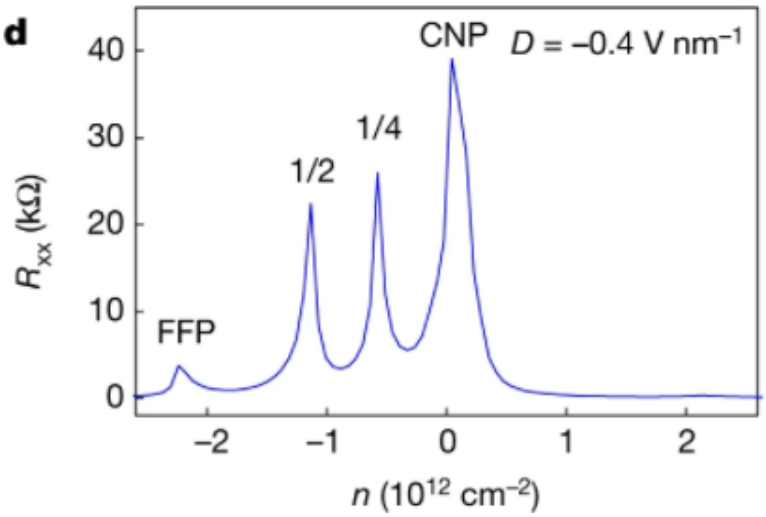

Figure 4.6: Rxx as a function of carrier density shows prominent Mott insulating states at 1/4 and 1/2 fillings with D =-0.4 V/nm at T = 5 K. [9]

4.2 Optical spectrum

4.2.1 Interband optical transitions at zero doping

At zero doping level, we observed strong optical absorption peak result from the van Hove singularities(vHS) of joint density of states(DOS).

In Fig.4.7, we calculated the band structure with six-band model of ABC-TLG. The dash line shows a gap-less band structure without an external displacement field, while the solid line shows a gaped band structure with the potential difference Δ between the top and bottom graphene layers. In the later case we can find that the first valance band is separated from all other bands resulting in a flat band which hosts strongly correlated physics when doped[8][15][16]. The band gap is slightly smaller than the potential difference Δ due to the potential energy asymmetry.

There are total of four possible optical transition within our interested energy range at zero doping level. I_1 is the transition from the first valance band to the first conduction band, which dominate the spectra because of the van Hove singularities(vHS) of joint density of states(DOS). When both conduction and valence bands are relatively flat as in our bandgap-opened TLG, the experimentally observed peak width serves as a good indicator of the single-particle bandwidth W. I_2 is the optical transition from the first valance band to the second conduction band, I_3 is the optical transition from the second valance band to the first conduction band, and I_4 is the optical transition from the second valance band to the second conduction band. Fig.4.8 shows the comparison between the calculated optical spectra and the experimental result. In the bottom panel, the calculated spectra at $\Delta = -87mV$ from different optical transitions are color-matched labeled corresponding to the color arrow in Fig.4.7, the black dashed curve is the sum of these four spectra. In the experimental data at $D = -0.71V/nm$, the main peak appears at around

72meV, a second broader peak shows up at around 95meV, which is consistent to the calculation result. Another sharp peak at around 102meV is due to the interlayer electron phonon coupling between hBN substrate and graphene, which is beyond the scope of this work and will be discussed elsewhere.

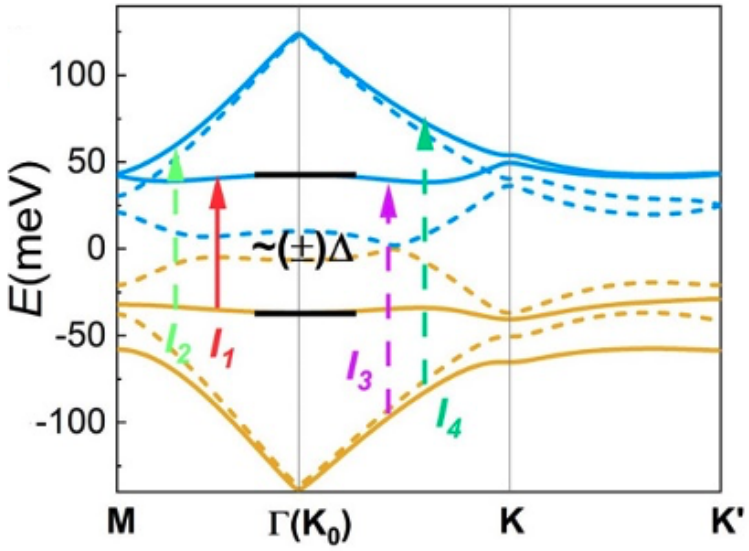

Figure 4.7: The calculation of the ABC-TLG band structure with six band model. The dashed line shows the dispersion without external displacement field, while the solid line shows the dispersion with a potential energy difference Δ between the top and the bottom layers of TLG.

Fig.4.9 shows the photocurrent spectra of TLG at different displacement field D, the charge density is fixed at zero by applying two opposite gate voltage at top and bottom gates. At $D = -0.38V/nm$, the photocurrent spectra has a broad peak at around 35meV. Because the band structure is dispersive at small displacement field, its full width at half-maximum (FWHM) is around 20 meV. As we increase the displacement field D from $-0.38V/nm$ to $-0.55V/nm$ and $-0.71V/nm$, this main peak turns to be sharper and moves to higher energy. Finally the peak width can reach as low as 5meV. At the opposite D direction, we observed a broad peak at $D = 0.33nm/V$, this peak becomes as sharp as 7meV at $D = 0.49V/nm$, and finally broadens again at $D = 0.66V/nm$, which shows a non-monotonic change of the peak width. The evolution of optical transition peak width largely reflected that of the single particle bandwidth W of the highest valence band. At the mean time, the second peak corresponding to I_3 and I_4 gradually emerges at both D directions.

Fig.4.10 is a 2D optical spectra color plot with a continuous D, it is more clear to trace the features evolution. Dashed lines indicate the position of the corresponding spectra in Fig.4.9 with the same color. We calculated optical conductivity spectra of the same device as a function of continuously tuned D, as shown in Fig.4.11. By aligning the lowest energy peak position in both experimental photocurrent spectrum and calculated optical conductivity spectrum, we established the relationship between D and Δ. In this way, we can

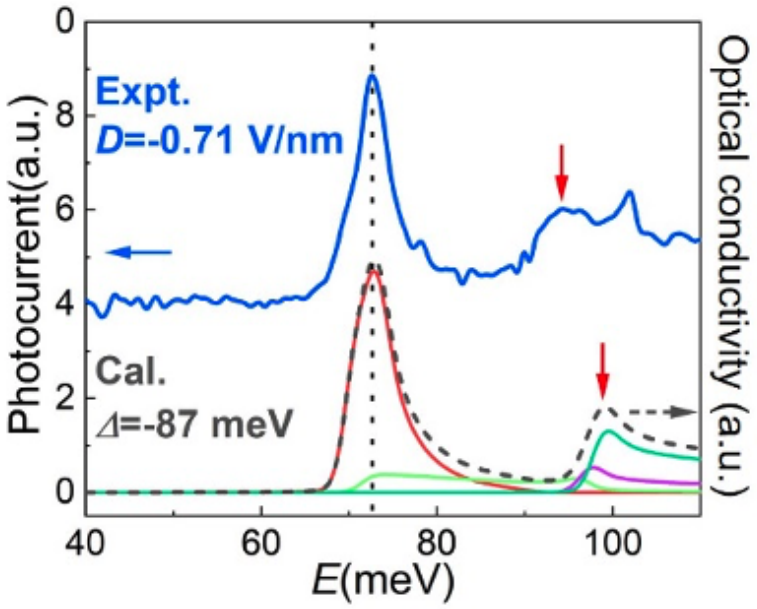

Figure 4.8: Comparison of the experimental and calculated spectra. Upper panel is the experimental spectra at $D = -0.71nm/V$. Lower panel plot the calculated spectra of the optical transition I_1, I_2, I_3, I_4 in Fig.4.7, respectively. The overall spectra is plotted with dashed line.

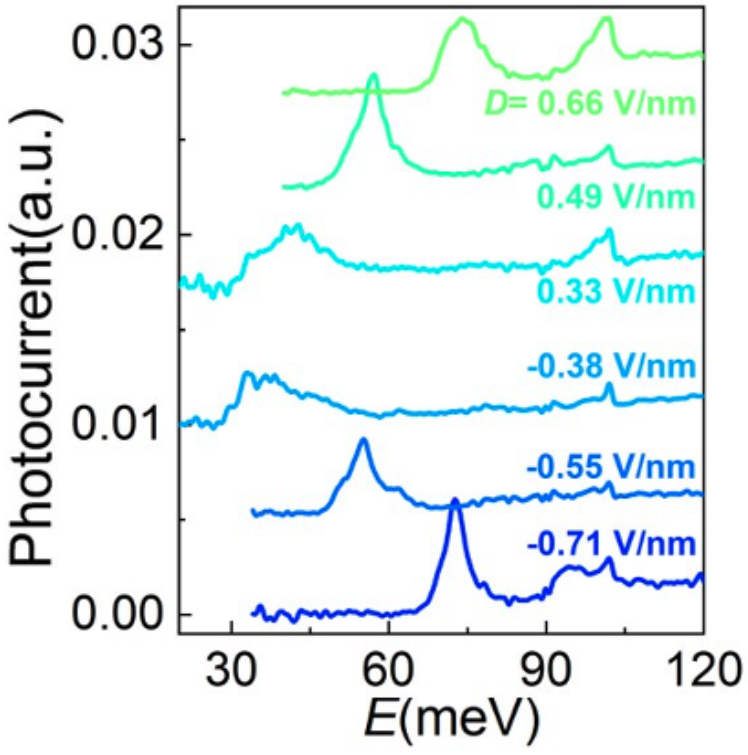

Figure 4.9: Photocurrent optical transition spectra at different displacement field D.

mark the corresponding experimental data region in Fig.4.11 with two white blocks. Major features and trends in Fig.4.10 agree with the result in the calculation as shown in Fig.4.11 pretty well. The blueshift of the I1-dominated optical transition peak indicates the opening of the bandgap. At the same time, thebandwidth of relevant moiré bands continually evolves.

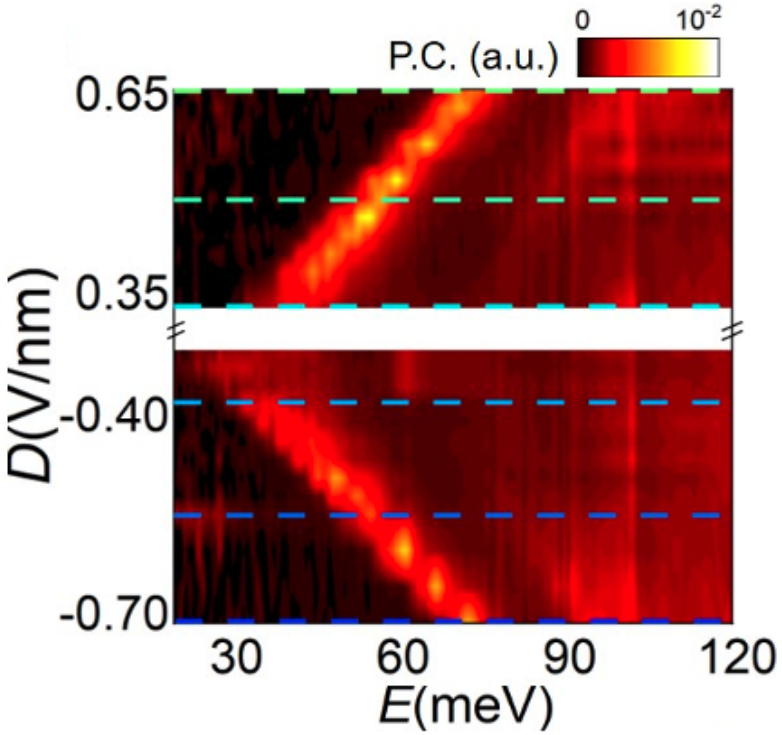

Figure 4.10: 2D color plot of the photocurrent spectra with continuous D.

In our data, we also oberved that with the same $|\Delta|$, the peak width for positive Δ is slightly broader than negative side as shown in Fig.4.12, this indicates that the negative side has a stronger correlation effect and agree with the transport data result[9].

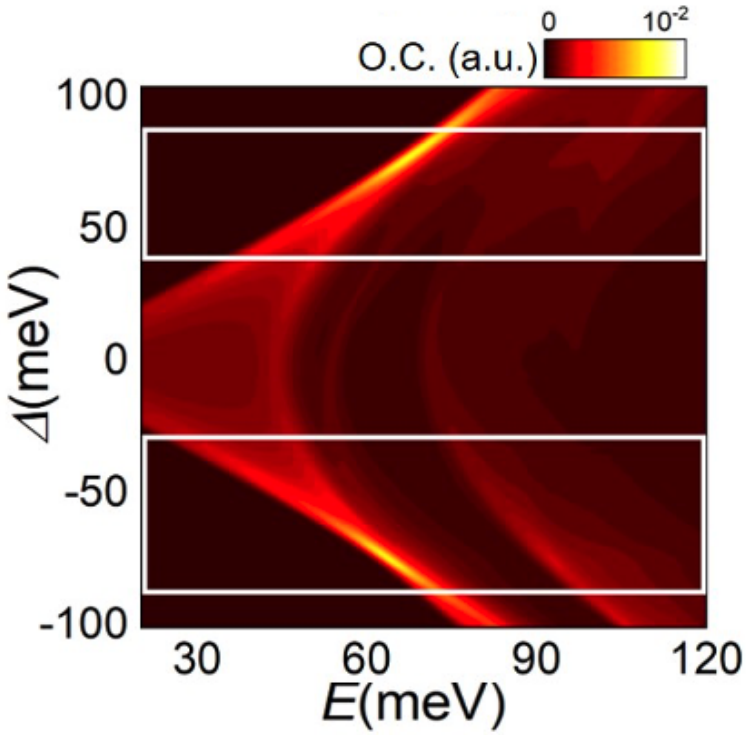

Figure 4.11: 2D color plot of the calculated spectra with continuous D, two white blocks indicate the corresponding region shown in the experimental 2D plot 4.10.

4.2.2 Optical transitions in the mott phase

According to our calculation, as the band gap was opened by the gate displacement field, the bandwidth W was suppressed and eventually approached around 12 meV, which is smaller than the estimated on-site Coulomb repulsion energy $U = \frac{e^2}{4\pi\epsilon_0\epsilon l_M} \approx 25meV$ ($l_M = 15nm$ is the moiré superlattice constant and $\epsilon = 4$ is the dielectric constant of hBN). This makes correlation effects possible when the sample is gated to partial doping level. In this section we focus on the optical transitions in the strongly correlated insulating state when the flat valence band is doped.

As we discussed in the previous section, at half-filling of the flat mini-valence band ($v = -1/2$), a correlated insulating state is formed as indicated by a resistance peak. Fig.4.13 shows the photocurrent spectrum at zero filling of this valance band at $D = -0.44V/nm$, there is a resonance peak at 45 meV with a 13meV FWHM, it's corresponding to the interband transition I_1 as indicated by the inset.

We examine the spectrum at a similar displacement field $D = -0.42V/nm$ with $v = -1/2$, the photocurrent spectrum is dramatically changed as shown in Fig.4.14. We observed a new strong optical resonance peak centered at around 18 meV. This energy is well below the bandgap energy in Fig.4.13, yet it is bigger than the DOS peak width of the flat valence band. The FWHM of this new peak is around 18 meV, which is significantly broader than the peak

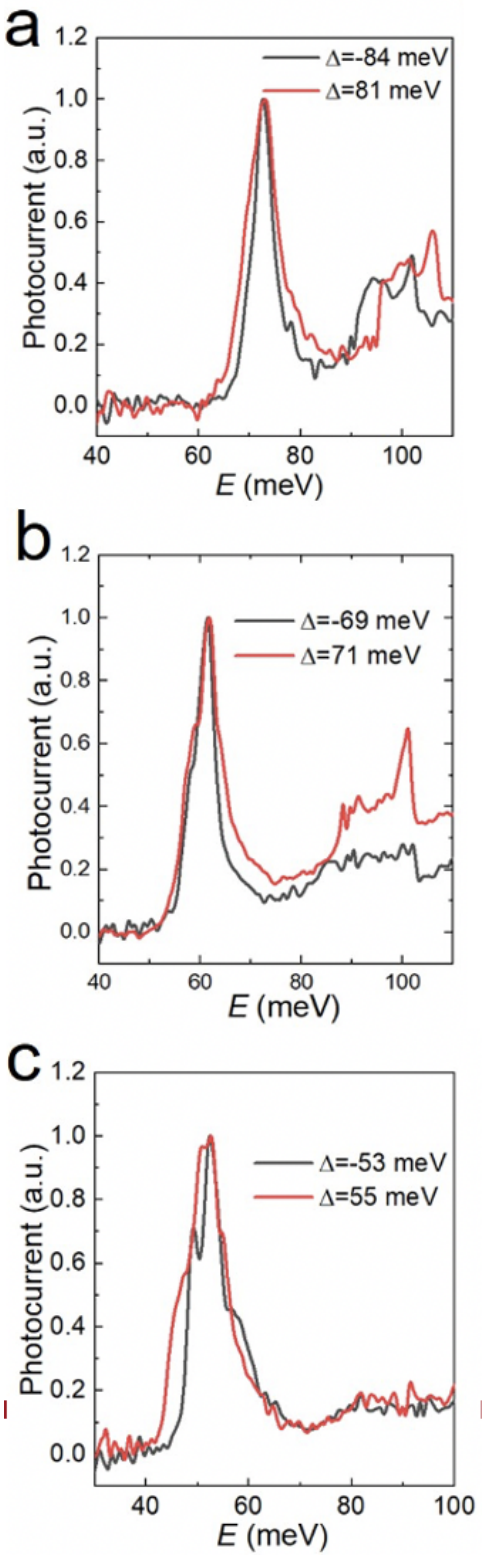

Figure 4.12: Comparison between the spectra of the positive and negative Δ at different $|\Delta|$ conditions. The positive spectra is always broader then the negative one.

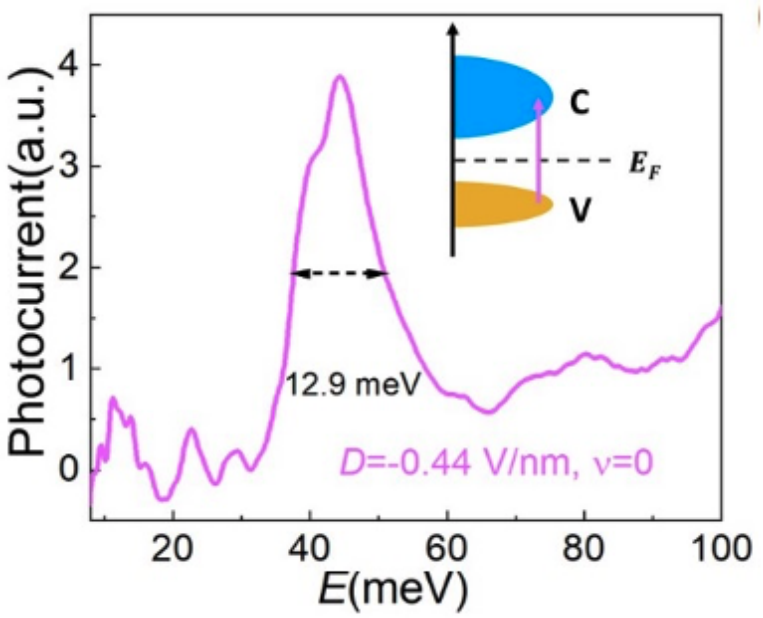

Figure 4.13: The photocurrent spectrum taken at $D = -0.44V/nm$, $v = 0$. The spectrum is dominated by a sharp peak at around 45 meV, which corresponds to the interband optical transition I_1 as illustrated by the inset.

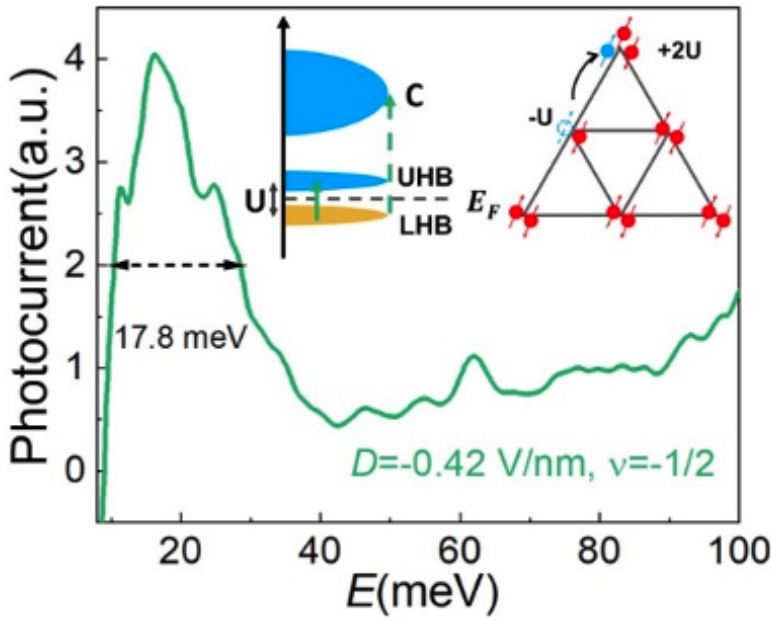

Figure 4.14: The photocurrent spectrum taken at $D = -0.42V/nm$, $v = -1/2$. a broad peak at around 18 meV emerges while the I1-dominated peak merges into the background. This low energy peak corresponds to optical transition across the Mott gap as illustrated by the left inset. The final state of such optical excitation contains a hole at one site and an extra electron at another site in the triangular moiré superlattice as illustrated in the right inset.

width in Fig.4.13. At the same time, the interband transition I_1-dominated peak is merged into the broad background.

These observations at $v = 1/2$ all indicate that the picture is much more complicated than in a doped trivial band insulator, in which the electron correlation effects can be neglected. For a half-doped single-band Hubbard model, theoretical calculations[17][18][19] predicted a broad peak in optical conductivity spectrum centering at around on-site Coulomb repulsion energy U. Such features have been observed by optical spectroscopy experiments in conventional strongly correlated materials[20][18]. We believe the strong peak at 18 meV in Fig.4.14 indicates formation of upper and lower Hubbard bands, with an optical transition across the Mott gap as illustrated by the inset of Fig.4.14, with the following 3 points.

1. In the final state of this optical excitation, a hole is created at one site while an extra electron is hopped to the neighbor site on the triangular moiré superlattice of TLG/hBN. For the moiré superlattice in our device, the onsite Coulomb repulsion energy U can be estimated by $\frac{e^2}{4\pi\epsilon_0\epsilon l_M} \approx 25meV$ [21]. This energy is close to the peak position of 18 meV in Fig.4.14 and bigger than the calculated single particle bandwidth of around 22 meV, which satisfying the condition of forming upper and lower Hubbard bands.

2. The second evidence of correlation effects is the dramatic broadening of the low energy peak. The FWMH of 18 meV is several times bigger than expected from simple uncorrelated band picture: without correlation, one expects a peak width of around 6.5 meV as deferred from experiment, and around 3.5 meV from calculation for the split bands (taking half of corresponding peak widths at $v = 0$).

3. The interband transition from the lower Hubbard band to the lowest conduction mini band (illustrated by the dashed arrow in the inset of Fig.4.14) can hardly be identified from the broad continuous background. It is likely that the DOS distribution of the lowest conduction band, which is remote to the flat valence band, also gets dramatically broadened and prevents an easy identification of the transition from the experimental spectrum. The broadening of both the flat band and remote band are similar to what happens in magic angle twist bilayer graphene(MATBLG)[7][4][6], implying strong correlation effects to play a key role.

Chapter 5

Conclusion

In this thesis, we provide spectroscopy evidence of the electron correlation effects in ABC-TLG/hBN morié superlattice. From the experimental data, we can extract the energy scales for the relevant parameters in the Hubbard model, which form the basis of accurate theoretical modeling and understanding of both observed[8][9] and predicted correlated ground states[21][22][23][24] in this moiré superlattice. Especially, we obtained the first optical spectrum in the Mott insulator states of all moiré superlattice systems. These observations open up opportunities to explore its doping and temperature dependence, sum rules of optical conductivity[25][18], and bound excitons of holon and doublon[24],[25]—all calling for further systematic study and theoretical calculations. On the other hand, the FTIR photocurrent spectroscopy technique employed here can be readily generalized to other (dual-)gated 2D moiré superlattice devices such as MATBLG, twisted double bilayer graphene, homo- and hetero-bilayers of transition metal dichalcogenides for better understanding of correlated electron physics in this designer material platform.

Reference

[1] A. K. Geim and K. S. Novoselov. "The rise of graphene". In: *Nature Materials* 6.3 (2007), pp. 183–191. ISSN: 14761122.

[2] Yuan Cao et al. "Correlated insulator behaviour at half-filling in magic-angle graphene superlattices". In: *Nature* 556.7699 (2018), pp. 80–84. ISSN: 14764687. DOI: 10.1038/nature26154. arXiv: 1802.00553.

[3] Yuan Cao et al. "Unconventional superconductivity in magic-angle graphene superlattices". In: *Nature* 556.7699 (2018), pp. 43–50. ISSN: 14764687. DOI: 10.1038/nature26160.

[4] Yonglong Xie et al. "Spectroscopic signatures of many-body correlations in magic-angle twisted bilayer graphene". In: *Nature* 572.7767 (2019), pp. 101–105. ISSN: 14764687. DOI: 10.1038/s41586-019-1422-x. arXiv: 1906.09274.

[5] Yuhang Jiang et al. "Charge order and broken rotational symmetry in magic-angle twisted bilayer graphene". In: *Nature* 573.7772 (2019), pp. 91–95. ISSN: 14764687. DOI: 10.1038/s41586-019-1460-4. arXiv: 1904.10153.

[6] Youngjoon Choi et al. "Electronic correlations in twisted bilayer graphene near the magic angle". In: *Nature Physics* 15.11 (2019), pp. 1174–1180. ISSN: 17452481. DOI: 10.1038/s41567-019-0606-5. arXiv: 1901.02997.

[7] Alexander Kerelsky et al. "Maximized electron interactions at the magic angle in twisted bilayer graphene". In: *Nature* 572.7767 (2019), pp. 95–100. ISSN: 14764687. DOI: 10.1038/s41586-019-1431-9.

[8] Guorui Chen et al. "Evidence of a gate-tunable Mott insulator in a trilayer graphene moiré superlattice". In: *Nature Physics* 15.3 (2019), pp. 237–241. ISSN: 17452481. DOI: 10.1038/s41567-018-0387-2.

[9] Guorui Chen et al. "Tunable correlated Chern insulator and ferromagnetism in a moiré superlattice". In: *Nature* 579.7797 (2020), pp. 56–61. ISSN: 14764687. DOI: 10.1038/s41586-020-2049-7.

[10] Long Ju et al. "Tunable excitons in bilayer graphene". In: *Science* 358.6365 (2017), pp. 907–910. ISSN: 10959203. DOI: 10.1126/science.aam9175.

[11] D. Cooper and et. al. D'Anjou B. "Effective mass of electrons and holes in bilayer graphene: Electron-hole asymmetry and electron-electron interaction". In: *ISRN Condensed Matter Physics* 2012 (1 Apr. 2012), p. 501686. DOI: 10.5402/2012/501686.

[12] Edward McCann and Mikito Koshino. "The electronic properties of bilayer graphene". In: *Reports on Progress in Physics* 76.5 (Apr. 2013), p. 056503. ISSN: 1361-6633. DOI: 10.1088/0034-4885/76/5/056503.

[13] F. Wang Y. Zhang et. al. "Direct observation of a widely tunable bandgap in bilayer graphene". In: *Nature* 459 (7248 June 2009), pp. 820–823. DOI: 10.1038/nature08105.

[14] Kin Fai Mak et al. "Optical spectroscopy of graphene: From the far infrared to the ultraviolet". In: *Solid State Communications* 152.15 (2012), pp. 1341–1349. ISSN: 00381098. DOI: 10.1016/j.ssc.2012.04.064.

[15] Bheema Lingam Chittari et al. "Gate-Tunable Topological Flat Bands in Trilayer Graphene Boron-Nitride Moiré Superlattices". In: *Phys. Rev. Lett.* 122 (1 Jan. 2019), p. 016401. DOI: 10.1103/PhysRevLett.122.016401.

[16] Ya-Hui Zhang et al. "Nearly flat Chern bands in moiré superlattices". In: *Phys. Rev. B* 99 (7 Feb. 2019), p. 075127. DOI: 10.1103/PhysRevB.99.075127.

[17] Elbio Dagotto. "Correlated electrons in high-temperature superconductors". In: *Rev. Mod. Phys.* 66 (3 July 1994), pp. 763–840. DOI: 10.1103/RevModPhys.66.763.

[18] Masatoshi Imada, Atsushi Fujimori, and Yoshinori Tokura. "Metal-insulator transitions". In: *Rev. Mod. Phys.* 70 (4 Oct. 1998), pp. 1039–1263. DOI: 10.1103/RevModPhys.70.1039.

[19] Eduardo Gagliano, Silvia Bacci, and Elbio Dagotto. "Hole motion in the t-J and Hubbard models: Effect of a next-nearest-neighbor hopping". In: *Phys. Rev. B* 42 (10 Oct. 1990), pp. 6222–6227. DOI: 10.1103/PhysRevB.42.6222.

[20] G. A. Thomas et al. "Observation of the Gap and Kinetic Energy in a Correlated Insulator". In: *Phys. Rev. Lett.* 73 (11 Sept. 1994), pp. 1529–1532. DOI: 10.1103/PhysRevLett.73.1529.

[21] Ya-Hui Zhang and T. Senthil. "Bridging Hubbard model physics and quantum Hall physics in trilayer graphene/$h-$BN moiré superlattice". In: *Phys. Rev. B* 99 (20 May 2019), p. 205150. DOI: 10.1103/PhysRevB.99.205150.

[22] Hoi Chun Po et al. "Origin of Mott Insulating Behavior and Superconductivity in Twisted Bilayer Graphene". In: *Phys. Rev. X* 8 (3 Sept. 2018), p. 031089. DOI: 10.1103/PhysRevX.8.031089.

[23] Cenke Xu and Leon Balents. "Topological Superconductivity in Twisted Multilayer Graphene". In: *Phys. Rev. Lett.* 121 (8 Aug. 2018), p. 087001. DOI: 10.1103/PhysRevLett.121.087001.

[24] J. van den Brink et al. "New Phases in an Extended Hubbard Model Explicitly Including Atomic Polarizabilities". In: *Phys. Rev. Lett.* 75 (25 Dec. 1995), pp. 4658–4661. DOI: 10.1103/PhysRevLett.75.4658.

[25] D. N. Basov et al. “Electrodynamics of correlated electron materials”. In: *Rev. Mod. Phys.* 83 (2 June 2011), pp. 471–541. DOI: 10.1103/RevModPhys.83.471.